

Exploring 2D/Quasi-2D Ruddlesden–Popper Perovskite $A_{n+1}Hf_nS_{3n+1}$ ($A = Ca, Sr,$ and $Ba; n = 1–3$) for Optoelectronics using Many-Body Perturbation Theory

Surajit Adhikari*, Aksaj Bharatwaj, and Priya Johari*

*Department of Physics, School of Natural Sciences,
Shiv Nadar Institution of Eminence, Greater Noida,
Gautam Buddha Nagar, Uttar Pradesh 201314, India.*

Dimensionality engineering in $A_{n+1}B_nX_{3n+1}$ Ruddlesden–Popper (RP) perovskite phases has emerged as a promising strategy to enhance optoelectronic properties. These properties are highly material-dependent, requiring detailed exploration of electronic, optical, excitonic, transport, and polaronic characteristics. However, the absence of comprehensive studies continues to impede the rational design of high-performance materials. In this work, we investigate the excitonic and polaronic effects in $A_{n+1}Hf_nS_{3n+1}$ ($A = Ca, Sr,$ and $Ba; n = 1–3$) RP phases, examining their relative stability and optoelectronic properties using several first-principles based methodologies within the framework of density functional theory and many-body perturbation theory (GW and BSE). Our study suggests that these compounds are mechanically stable and feature $G_0W_0@PBE$ bandgaps ranging from 1.43 to 2.14 eV, which are smaller than those of their bulk counterparts. BSE and model-BSE (mBSE) calculations indicate that these RP phases display notable optical anisotropy, with the exciton binding energy decreasing as the thickness of the perovskite layer increases. In addition, intermediate to strong carrier-phonon scattering is observed in these compounds, confirmed through the Fröhlich mechanism near room temperature. Using the Feynman polaron model, the polaron parameters of these RP phases are also computed, and it is found that charge-separated polaronic states are less stable than bound excitons. Finally, a significant increase in electron mobilities is observed in RP phases compared to their bulk counterparts. Overall, the insights gained from this study will enable the rational design of layered perovskite phases for applications in solar cells and other optoelectronic devices.

I. INTRODUCTION:

Lead halide perovskites $APbX_3$ [$A = Cs^+, CH_3NH_3^+, CH(NH_2)_2^+$; $X = Cl^-, Br^-, I^-$] have gained immense attention for their applications in optoelectronic and solar cell, owing to their exceptional electronic and optical properties, high carrier mobility, low production cost, and outstanding power conversion efficiency [1–5]. However, the inclusion of organic components in these materials compromises their stability, making them susceptible to degradation from heat, light, and moisture, which adversely affects their long-term performance. Additionally, the toxicity of lead raises serious environmental and health concerns, further limiting their practical applications [6, 7].

Seeking alternatives to overcome the limitations of lead halide perovskites, chalcogenide perovskites (CPs) with sulfur (S) or selenium (Se) anions have emerged as promising candidates for photovoltaic applications [8–11]. Several prototypical distorted CPs, such as ABS_3 ($A = Ca, Sr, Ba; B = Zr, Hf$), have been successfully synthesized and theoretically explored for photovoltaic applications [12–14]. Among these, Hf-based compounds exhibit higher bandgaps (2.17–2.46 eV), lower charge carrier mobility (9.44–15.68 $cm^2V^{-1}s^{-1}$), and reduced power conversion efficiency (10.56–13.26%), which collectively constrain the photovoltaic performance of Hf-based CPs [13, 14]. To enhance solar cell performance, alloying/doping at the Hf and S sites has been explored in these materials [15–17]. Alloying is a widely used method to modulate the bandgap of semiconductors; however, the resulting disorder often leads to a reduction in carrier mobility [18, 19]. Furthermore, doped or alloyed configurations tend to encounter stability issues [20].

Ruddlesden–Popper (RP) phases offer an alternative strategy for achieving long-range ordered structures, enabling precise tuning of electronic and optical properties [21]. The RP phases, resembling the perovskite structure, are developing as semiconductors for optoelectronic applications [21, 22]. The general formula of RP phases is $A_{n+1}B_nX_{3n+1}$ or $AX[ABX_3]_n$, where perovskite structure blocks with a unit cell thickness of “ n ” are separated by a rock salt layer (AX) along the [001] direction [21]. The alternate perovskite blocks are displaced in the in-plane direction by half of the unit cell. One of the key advantages of RP phases is the tunable dimensionality parameter, n , which offers enhanced flexibility in modifying the bandgap, chemical stability, and charge transport properties, compared to their

* sa731@snu.edu.in, priya.johari@snu.edu.in

bulk counterparts ABX_3 ($n = \infty$) [21–24]. The bandgap is particularly crucial in determining the practical performance and efficiency of RP phases in optoelectronic devices, which has led to extensive research aimed at modulating the bandgap through dimensionality engineering.

The RP phases are classified under the broad category of “2D perovskites” due to their layered structural arrangement, where the periodic stacking of perovskite layers creates a bulk structure (see Figure 1). Their material properties can be tuned through substitution or dimensional reduction. For example, previous theoretical study indicated that the bandgaps of $Ba_{n+1}Zr_nS_{3n+1}$ ($n = 1–3$) RP phases are significantly lower than that of the parent perovskite, $BaZrS_3$ [21, 23]. Due to quantum confinement effects, reducing the dimensionality of the material leads to significant changes in its physical properties and the evolution of the bandgap [21, 25].

Inspired by the dimensionality engineering of RP phases for developing efficient materials for photovoltaic and other optoelectronic applications, this work aims to investigate the optoelectronic properties along with excitonic and polaronic effects in $A_{n+1}Hf_nS_{3n+1}$ ($A = Ca, Sr, \text{ and } Ba; n = 1–3$) RP phases within the framework of density functional theory (DFT) [26, 27] and many-body perturbation theory (MBPT) [28, 29]. Initially, we optimized the crystal structures using the semilocal PBE exchange–correlation (xc) functional [30] and assessed their stability. To investigate the electronic properties, band structures are calculated using both the HSE06 functional [31] and the $G_0W_0@PBE$ method [32, 33]. Subsequently, the optical properties are determined using the Bethe–Salpeter equation (BSE) [34, 35] and model-BSE (mBSE) [36] methods. In addition, the BSE/mBSE method and the Wannier-Mott model [37] are employed to compute the excitonic properties of these compounds, as exciton formation in optoelectronic materials significantly impacts their charge-separation characteristics. Polaronic effects are also suggested to play a crucial role in excitation dynamics and carrier transport. Consequently, electron-phonon coupling is addressed using the Frohlich model, and polaron mobility is computed using the Hellwarth polaron model [38]. Overall, this paper demonstrates that dimensionality engineering in $A_{n+1}Hf_nS_{3n+1}$ ($A = Ca, Sr, \text{ and } Ba; n = 1–3$) RP phases offers a promising strategy for developing efficient materials for optoelectronic devices.

II. COMPUTATIONAL DETAILS:

The first-principles calculations were carried out using the projected augmented wave (PAW) [39] method as implemented in the Vienna Ab initio Simulation Package (VASP) [40, 41]. The generalized gradient approximation (GGA) based Perdew–Burke–Ernzerhof (PBE) exchange–correlation (xc) functional [30] was employed for structural optimizations, effectively incorporating electron–electron interactions. The valence electronic configurations considered for Ca, Sr, Ba, Hf, and S were $3s^23p^64s^2$, $4s^24p^65s^2$, $5s^25p^66s^2$, $5p^66s^25d^2$, and $3s^23p^4$, respectively. A $2 \times 2 \times 2$ Γ -centered k -point mesh was utilized, and the plane-wave cutoff energy was set to 400 eV for optimization calculations. Full structural relaxation was performed with the electronic self-consistent-field (SCF) iteration energy convergence criterion of 10^{-6} eV and the Hellmann–Feynman force convergence criterion set to 0.01 eV/Å. The crystal structures were visualized using the VESTA software [42]. The advanced hybrid HSE06 [31] xc functional and MBPT-based GW ($G_0W_0@PBE$) [32, 33] calculations were performed to obtain a more precise estimation of the electronic bandgap. The effective mass was calculated using the Sumo-bandstat program [43]. To explore the optical properties and excitonic effects, the Bethe–Salpeter equation (BSE) [34, 35] was solved on top of the $G_0W_0@PBE$ calculation, explicitly incorporating the electron-hole interaction. A Γ -centered $2 \times 2 \times 2$ k -grid and a converged NBANDS of 800 were employed for the GW-BSE calculations. The electron–hole kernel for the BSE calculations was constructed using 8 occupied and 8 unoccupied bands. However, for $A_4Hf_3S_{10}$ ($A = Ca, Sr, Ba$) compounds, performing BSE calculations was infeasible due to computational limitations, even with the fastest supercomputers. To address this challenge, a less computationally demanding yet reliable model-BSE (mBSE) [36] approach was utilized for these compounds. Following this, the ionic contribution to the dielectric constant was calculated using the DFPT method [44].

III. RESULTS AND DISCUSSIONS:

In this study, we conducted a comprehensive and systematic investigation of the Ruddlesden–Popper (RP) phases $A_{n+1}Hf_nS_{3n+1}$ ($A = Ca, Sr, \text{ and } Ba; n = 1–3$) to explore their potential optoelectronic features. The subsequent sections present an in-depth analysis of their stability, as well as their structural, electronic, optical, excitonic, and polaronic properties, providing valuable insights to guide and inspire future experimental research.

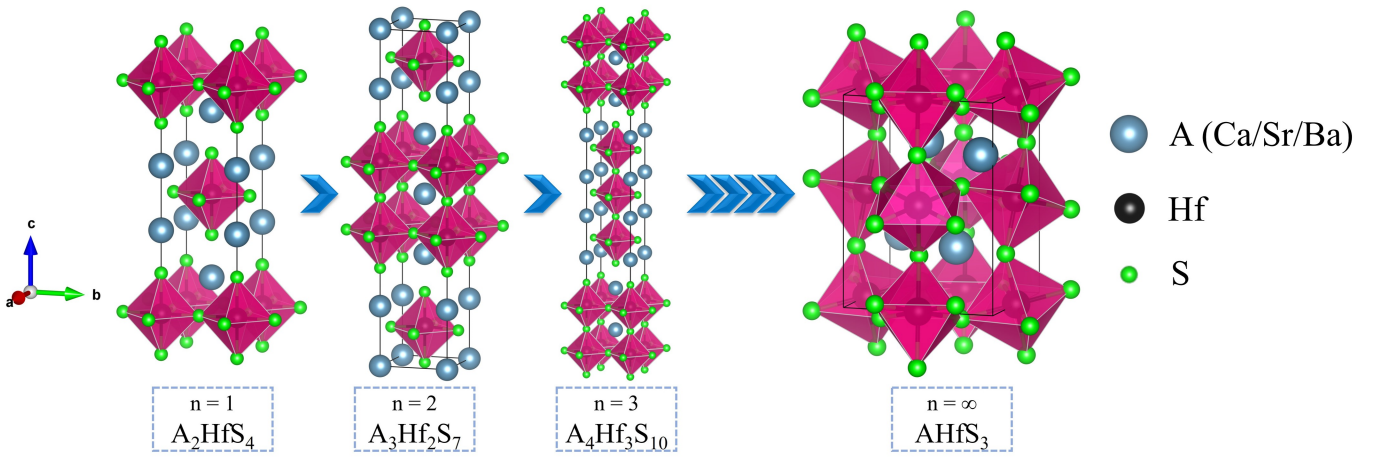


Figure 1. Optimized crystal structure of $A_{n+1}\text{Hf}_n\text{S}_{3n+1}$ ($A = \text{Ca}, \text{Sr}, \text{Ba}$ and $n = 1-3$) RP phases.

A. Structural Properties:

Ruddlesden–Popper phases of chalcogenide perovskites follow the general formula $\text{AX}[\text{ABX}_3]_n$, where ABX_3 perovskite blocks (P-blocks) are stacked along the $[001]$ direction. For every n perovskite units, an additional AX layer is inserted, and the interlayer A cations coordinate with the terminal chalcogen (X) atoms, forming rock-salt blocks (R-blocks) [45]. Figure 1 illustrates the crystal structures of the $A_{n+1}\text{Hf}_n\text{S}_{3n+1}$ ($A = \text{Ca}, \text{Sr}, \text{Ba}$ and $n = 1-3$) RP phases. The calculated lattice parameters of these RP phases are tabulated in Table I, confirm that they adopt a tetragonal structure with the space group $I4/mmm$ (No. 139). To validate the accuracy of the current method for determining the structural parameters of these RP phases, we also examined the structural properties of the parent materials, specifically bulk AHfS_3 ($n = \infty$), where $A = \text{Ca}, \text{Sr}$, and Ba . It is found that the relaxed lattice parameters of these parent materials are in excellent agreement with the experimental values [14]. For example, the experimental lattice parameters of SrHfS_3 are $a = 6.72 \text{ \AA}$, $b = 7.05 \text{ \AA}$, and $c = 9.72 \text{ \AA}$, which closely align with our theoretical values. This agreement validates the reliability of the PBE method in accurately describing the structural properties of RP perovskites.

Table I. Calculated lattice parameters a , b , and c (in unit \AA) of $A_{n+1}\text{Hf}_n\text{S}_{3n+1}$ ($A = \text{Ca}, \text{Sr}, \text{Ba}$; $n = 1-3$) RP phases and AHfS_3 ($A = \text{Ca}, \text{Sr}, \text{Ba}$; $n = \infty$) chalcogenide perovskites.

Configurations	$n = 1$	$n = 2$	$n = 3$	$n = \infty$
$\text{Ca}_{n+1}\text{Hf}_n\text{S}_{3n+1}$	$a = b = 4.90,$ $c = 14.36$	$a = b = 4.93,$ $c = 23.85$	$a = b = 4.94,$ $c = 33.78$	$a = 6.56, b = 7.01,$ $c = 9.58$
$\text{Sr}_{n+1}\text{Hf}_n\text{S}_{3n+1}$	$a = b = 4.91,$ $c = 15.13$	$a = b = 4.95,$ $c = 24.81$	$a = b = 4.97,$ $c = 34.67$	$a = 6.76, b = 7.10,$ $c = 9.77$
$\text{Ba}_{n+1}\text{Hf}_n\text{S}_{3n+1}$	$a = b = 4.96,$ $c = 15.86$	$a = b = 4.99,$ $c = 25.75$	$a = b = 5.03,$ $c = 35.63$	$a = 7.03, b = 7.09,$ $c = 9.99$

To assess the stability of these RP phases, their mechanical stability and associated elastic properties have also been analyzed. The elastic properties are computed by determining the second-order elastic constants (C_{ij}) using the energy-strain approach [46]. Since all the RP phases considered in this study exhibit tetragonal (I) symmetry, six independent elastic coefficients— C_{11} , C_{33} , C_{44} , C_{66} , C_{12} , and C_{13} —are required to explain the mechanical stability and corresponding elastic properties of these systems. Using these elastic constants, we can calculate the bulk modulus (B), shear modulus (G), Young’s modulus (Y), and Poisson’s ratio (ν) of the perovskites (for details, see the Supplemental Material). The corresponding mechanical stability criterion is expressed as follows [46]:

$$C_{11} > |C_{12}|, 2C_{13}^2 < C_{33}(C_{11} + C_{12}), C_{44} > 0, C_{66} > 0 \quad (1)$$

The calculated elastic constants and moduli are provided in Table II. As shown, the elastic constants meet the Born stability criteria, confirming the mechanical stability of these RP phases. Pugh’s suggested B/G ratio and

Poisson's ratio (ν) are used to study the fragility of the materials [47]. A material is considered ductile if B/G is greater than 1.75 and (ν) exceeds 0.26; otherwise, it is brittle. The calculated values of B/G and (ν) indicate that the studied compounds exhibit ductile behavior. These specific elastic properties make the selected RP phases ideal for applications in flexible and durable devices.

Table II. Mechanical parameters for RP phases, including elastic constants C_{ij} (in GPa), bulk modulus B (in GPa), shear modulus G (in GPa), Young's modulus Y (in GPa), and Poisson's ratio ν (dimensionless).

Configurations	C_{11}	C_{33}	C_{44}	C_{66}	C_{12}	C_{13}	B	G	Y	B/G	ν	
$\text{Ca}_{n+1}\text{Hf}_n\text{S}_{3n+1}$	$n = 1$	130.20	121.70	24.00	15.41	26.63	41.36	66.74	28.38	74.56	2.35	0.31
	$n = 2$	133.24	112.47	20.02	21.92	30.00	37.76	65.47	28.45	74.55	2.30	0.31
	$n = 3$	125.91	93.18	17.46	29.55	29.26	39.02	61.86	26.76	70.16	2.31	0.31
$\text{Sr}_{n+1}\text{Hf}_n\text{S}_{3n+1}$	$n = 1$	130.03	116.23	23.98	19.61	25.25	37.45	64.06	29.95	77.74	2.14	0.30
	$n = 2$	133.92	112.19	24.04	24.30	28.09	37.86	65.23	31.25	80.85	2.09	0.29
	$n = 3$	125.15	110.56	21.39	30.35	31.33	39.43	64.56	29.95	77.82	2.16	0.30
$\text{Ba}_{n+1}\text{Hf}_n\text{S}_{3n+1}$	$n = 1$	121.09	107.77	25.46	24.72	24.94	31.09	58.22	31.46	79.98	1.85	0.27
	$n = 2$	132.43	116.91	29.21	28.53	29.64	35.38	64.69	35.13	89.23	1.84	0.27
	$n = 3$	123.13	114.50	23.51	34.74	32.44	34.67	62.68	32.40	82.92	1.93	0.28

B. Electronic properties:

After evaluating the stability of the $\text{A}_{n+1}\text{Hf}_n\text{S}_{3n+1}$ ($\text{A} = \text{Ca}, \text{Sr}, \text{Ba}; n = 1-3$) RP phases, their electronic band structures are calculated, which play a crucial role in the design of photoelectric devices. Initially, the band structures are computed using the semi-local PBE xc functional, both with and without considering the spin-orbit coupling (SOC) effect. However, it is well-known that the PBE functional struggles to accurately predict the bandgaps of chalcogenide perovskites due to its inability to account for the self-interaction error of electrons [13, 48]. Additionally, the inclusion of SOC has no significant impact on the bandgaps (For details, see the Table S1). To achieve more accurate results, hybrid HSE06 functional (with 25% exact exchange and a screening parameter of 0.2 \AA^{-1}) and the MBPT-based G_0W_0 @PBE method are employed for bandgap calculations. The band structures calculated using G_0W_0 @PBE method are presented in Figure 2, while those obtained with the HSE06 functional are shown in Figure S1. Our results show that all the RP phases display indirect bandgaps, with the conduction band minimum (CBM) located at the Γ (0, 0, 0) point and the valence band maximum (VBM) situated at the X (0, 0, 0.5) point of the Brillouin zone. The HSE06 and G_0W_0 @PBE estimated bandgaps of these RP phases are listed in Table III, showing that the bandgaps of these compounds decrease as the thickness of the perovskite layer (n) increases. The bandgap of these RP phases, computed using HSE06 and G_0W_0 @PBE, lies within the ranges of 1.02–1.66 eV and 1.43–2.14 eV, respectively. This implies that all of these RP phases have smaller bandgaps compared to their bulk counterparts, such as AHfS_3 ($n = \infty$, where $\text{A} = \text{Ca}, \text{Sr}, \text{Ba}$) [13, 24]. For example, CaHfS_3 perovskite has a G_0W_0 @PBE bandgap of 2.46 eV, which is significantly higher than the bandgaps of the $\text{Ca}_{n+1}\text{Hf}_n\text{S}_{3n+1}$ ($n = 1-3$) RP phases. This property suggests that these RP phases could be promising candidates for optoelectronic technologies.

Table III. Bandgap (in eV) of RP phases calculated using PBE, HSE06 and G_0W_0 @PBE method. Also, effective masses of electron (m_e^*), hole (m_h^*), and reduced mass (μ^*) of RP phases calculated using G_0W_0 @PBE method.

Configurations	PBE	HSE06	G_0W_0 @PBE	m_e^* (m_0)	m_h^* (m_0)	μ^* (m_0)	
$\text{Ca}_{n+1}\text{Hf}_n\text{S}_{3n+1}$	$n = 1$	0.32	1.08	1.55	0.179	0.573	0.136
	$n = 2$	0.30	1.05	1.53	0.182	1.683	0.164
	$n = 3$	0.24	1.02	1.43	0.192	0.537	0.141
$\text{Sr}_{n+1}\text{Hf}_n\text{S}_{3n+1}$	$n = 1$	0.61	1.38	1.89	0.177	0.726	0.142
	$n = 2$	0.55	1.31	1.76	0.179	2.365	0.166
	$n = 3$	0.46	1.28	1.61	0.187	0.597	0.142
$\text{Ba}_{n+1}\text{Hf}_n\text{S}_{3n+1}$	$n = 1$	0.87	1.66	2.14	0.185	0.868	0.152
	$n = 2$	0.75	1.52	1.90	0.183	3.880	0.175
	$n = 3$	0.55	1.37	1.62	0.192	0.600	0.145

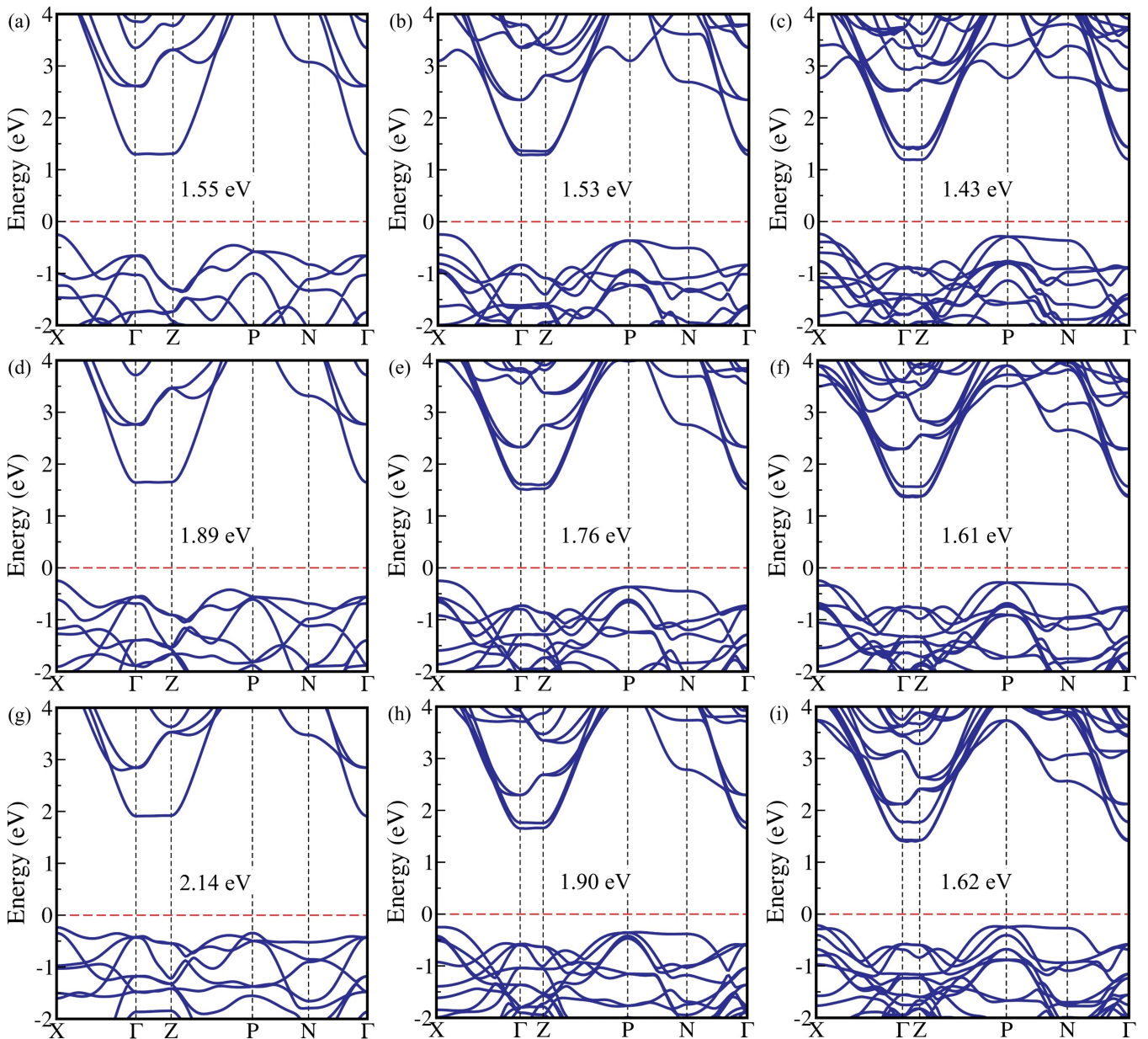


Figure 2. Band structures of (a–c) $\text{Ca}_{n+1}\text{Hf}_n\text{S}_{3n+1}$, (d–f) $\text{Sr}_{n+1}\text{Hf}_n\text{S}_{3n+1}$, and (g–i) $\text{Ba}_{n+1}\text{Hf}_n\text{S}_{3n+1}$, respectively, where $n = 1–3$, calculated using the $G_0W_0@PBE$ method.

To gain deeper insight into charge carrier transport, we further calculated the effective masses of electrons (m_e^*) and holes (m_h^*) for all the RP phases. This is achieved by fitting the $E - k$ dispersion from the $G_0W_0@PBE$ band structures and applying the formula: $m^* = \hbar^2 [\partial^2 E(k)/\partial k^2]^{-1}$, where \hbar is the reduced Planck's constant. In this study, we computed the effective masses of electrons and holes along the symmetric paths $\Gamma \rightarrow X$ and $X \rightarrow \Gamma$, respectively. The obtained values of the effective mass and reduced mass, expressed in terms of the rest mass of an electron (m_0), for the RP phases are listed in Table III. Also, it is found that the electron effective masses of these RP phases increase with the value of n , whereas the hole effective masses exhibit an oscillating behavior. Overall, these results suggest that the RP phases are likely to exhibit higher charge carrier mobility for electrons compared to holes.

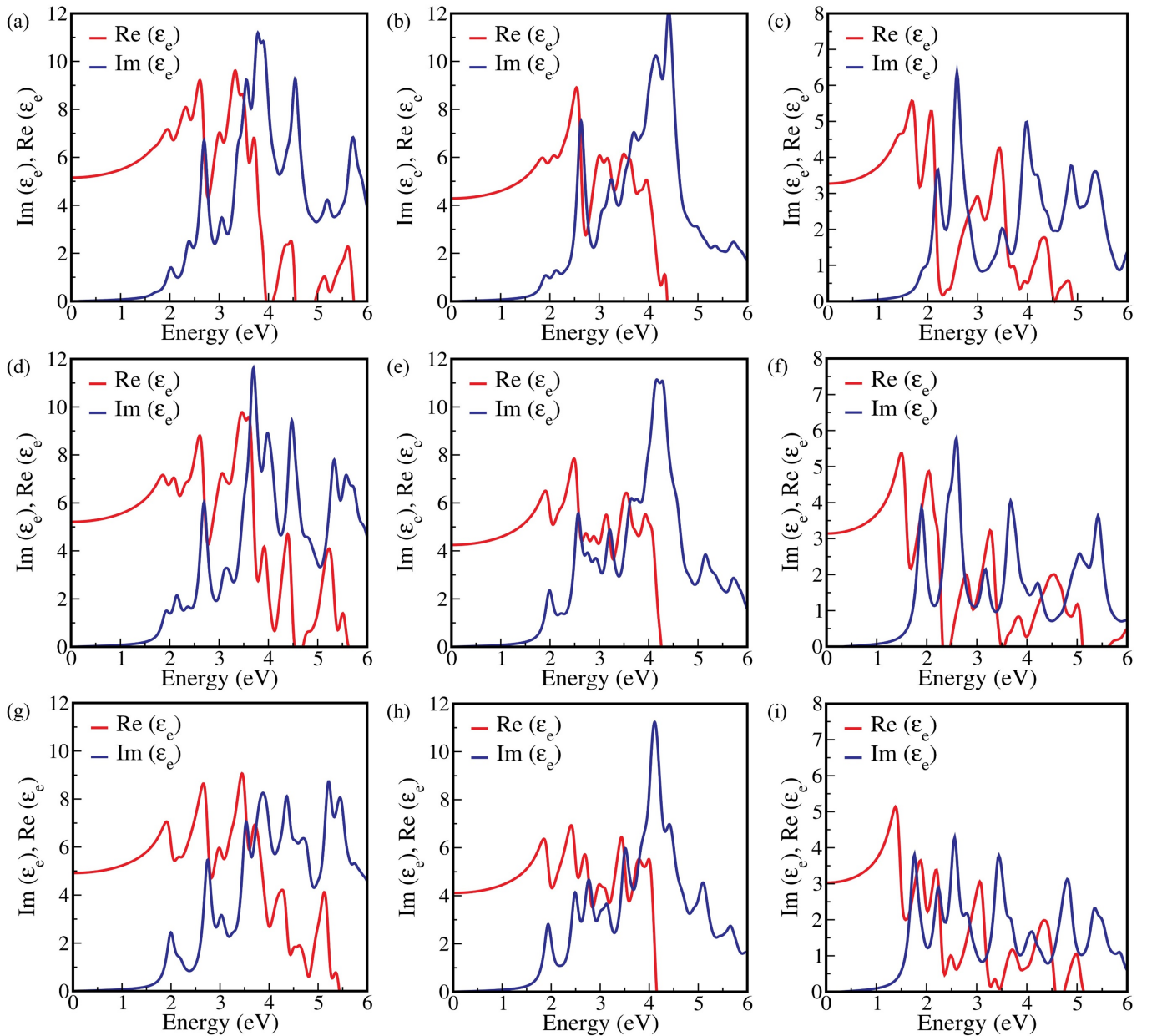


Figure 3. Real [$\text{Re}(\epsilon)$] and imaginary [$\text{Im}(\epsilon)$] parts of the dielectric (electronic) function for (a–c) $\text{Ca}_{n+1}\text{Hf}_n\text{S}_{3n+1}$, (d–f) $\text{Sr}_{n+1}\text{Hf}_n\text{S}_{3n+1}$, and (g–i) $\text{Ba}_{n+1}\text{Hf}_n\text{S}_{3n+1}$, where $n = 1-3$, computed using the BSE@ G_0W_0 @PBE ($n = 1, 2$) and mBSE@ G_0W_0 @PBE ($n = 3$) methods, respectively.

C. Optical Properties:

Although most of these compounds exhibit lower bandgaps and low effective carrier masses, these properties alone are insufficient to guarantee their suitability for optoelectronic device applications. Therefore, we investigated the optical response of the $\text{A}_{n+1}\text{Hf}_n\text{S}_{3n+1}$ ($\text{A} = \text{Ca}, \text{Sr}, \text{Ba}; n = 1-3$) RP phases by calculating the real [$\text{Re}(\epsilon)$] and imaginary [$\text{Im}(\epsilon)$] parts of the dielectric function. To achieve higher reliability in optical response estimation, the Bethe-Salpeter Equation (BSE) was solved on top of G_0W_0 @PBE, explicitly accounting for excitonic effects (electron-hole interactions) [34, 35]. However, for $n = 3$ in the RP phases, performing BSE calculations has been computationally infeasible, even with the most advanced supercomputers. To address this limitation, a parametrized model for dielectric screening, known as the model-BSE (mBSE) approach [36], has been employed for these compounds. This mBSE approach is computationally less expensive compared to the full BSE, while maintaining similar accuracy in

estimating the first peak position (for details, see the Supplemental Material).

Figure 3 represents the average optical responses, including the real and imaginary components of the electronic dielectric function, calculated along the x , y , and z directions for these RP phases. However, Figure S3[(a)-(c)] and Figure S3 [(d)-(f)] illustrate the directional optical responses of the RP phases along the $E||xy$ (i.e., in-plane along the x or y directions) and $E||z$ (i.e., out-of-plane along the z direction) directions, respectively. The directional optical responses exhibit significant optical anisotropy in these compounds, which could have a substantial impact on their performance in practical applications. Figure 3 reveals that the absorption onset of these compounds shows a gradual redshift with an increase in the thickness of the perovskite layers. Additionally, the optical peak position (E_o) of these compounds varies with the n value, which is crucial for determining the exciton binding energy. For example, the optical peak position of Ba_2HfS_4 is 2 eV, while those of $\text{Ba}_3\text{Hf}_2\text{S}_7$ and $\text{Ba}_4\text{Hf}_3\text{S}_{10}$ are 1.94 eV and 1.76 eV, respectively. Similarly, the peak positions of $\text{Ca}_{n+1}\text{Hf}_n\text{S}_{3n+1}$ and $\text{Sr}_{n+1}\text{Hf}_n\text{S}_{3n+1}$ varies in between 1.72–1.91 eV and 1.89–1.99 eV, respectively. It should be emphasized that all the compounds exhibit absorption onsets within the visible region, making them well-suited for optoelectronic applications.

D. Excitonic Properties:

In optoelectronic materials, exciton generation significantly influences charge separation properties. Consequently, excitonic parameters, such as exciton binding energy (E_B) and exciton lifetime (τ_{exc}), serve as critical descriptors for evaluating and optimizing their performance in various applications. The exciton binding energy (E_B) is defined as the energy required to dissociate an exciton into its constituent electron (e) and hole (h) pair. The value of E_B is calculated using the Wannier–Mott model, which assumes a simple screened Coulomb potential to describe the interaction between the electron and hole in a material [23]. Recent studies have reported that excitons in the RP phases of MAPbX_3 are significantly influenced by quantum confinement effects along the z -direction, leading to a quasi-2D character [37]. In our case, we observe differences in the spectra along the xy and z directions, indicating weak hybridization along the z -direction. Also, increasing the number of perovskite layers leads to deviations from ideal 2D behavior, attributed to the screened Coulomb potential [23, 37]. Therefore, For $n = 1$ and 2, the 2D Wannier–Mott model is more applicable, while for $n = 3$ and above, the 3D model may also be relevant. Thus, according to the 2D Wannier–Mott model, the E_B of the RP phases is calculated as [23, 37],

$$E_B = \frac{1}{\left(n - \frac{1}{2}\right)^2} \left(\frac{\mu^*}{\varepsilon_{\text{eff}}^2}\right) R_\infty \quad (2)$$

where μ^* is the reduced mass of the charge carriers at the direct band edges, m_0 is the rest mass of the electron, ε_{eff} denotes the effective dielectric constant, and R_∞ is the Rydberg constant. The reduced masses for the RP phases at direct band edges are provided in Table S2 of the Supplemental Material. However, ε_{eff} is unknown for these RP phases. According to previous reports, E_B is influenced by lattice relaxation [49], and if $E_B \ll \hbar\omega_{LO}$, lattice relaxation must be considered, where ω_{LO} denotes the longitudinal optical phonon frequency. Therefore, in determining ε_{eff} , a value intermediate between the electronic (ε_∞) and static ($\varepsilon_s = \varepsilon_\infty + \varepsilon_i$) dielectric constants should be considered, where ε_i representing the ionic contribution to the dielectric function. The values of ε_∞ and ε_i are obtained using the BSE/mBSE and DFPT methods, respectively. On the other hand, if $E_B \gg \hbar\omega_{LO}$, the ionic dielectric constant becomes negligible, and $\varepsilon_{\text{eff}} \rightarrow \varepsilon_\infty$, indicating that the static dielectric constant is primarily determined by the electronic contribution at high frequency [36, 50]. Using the electronic and static dielectric constants, along with Equation 2, we have calculated the upper (E_{Bu}) and lower (E_{Bl}) bounds of the exciton binding energy (see Table IV). The results indicate that the upper bounds of E_B show a significant reduction in exciton binding energies for the examined RP phases as the thickness of the perovskite layer (n) increases. In the absence of experimental data, we have also conducted a theoretical analysis based on the 3D Wannier–Mott excitons (for details, see the Supplemental Material).

Table IV. Exciton binding energy of $A_{n+1}\text{Hf}_n\text{S}_{3n+1}$ ($A = \text{Ca}, \text{Sr}, \text{Ba}$ and $n = 1-3$) RP phases using Wannier-Mott Model.

Configurations	ε_∞	E_{Bu} (meV)	ε_s	E_{Bl} (meV)	
$\text{Ca}_{n+1}\text{Hf}_n\text{S}_{3n+1}$	$n = 1$	5.46	218.98	17.51	21.29
	$n = 2$	4.35	38.97	22.71	1.43
	$n = 3$	2.03	89.23	22.59	0.72
$\text{Sr}_{n+1}\text{Hf}_n\text{S}_{3n+1}$	$n = 1$	5.62	218.74	42.22	3.88
	$n = 2$	4.42	40.22	136.58	0.04
	$n = 3$	2.06	74.35	17.78	1.00
$\text{Ba}_{n+1}\text{Hf}_n\text{S}_{3n+1}$	$n = 1$	5.22	309.45	47.68	3.71
	$n = 2$	4.34	51.99	92.70	0.11
	$n = 3$	2.15	77.20	274.79	0.005

In addition to the Wannier-Mott model, we computed the first-principles exciton binding energies (E_B) for these RP phases using the BSE (for $n = 1, 2$) and mBSE (for $n = 3$) methods. The binding energy is defined as, $E_B = E_g^{dir} - E_o$, where E_g^{dir} is the direct G_0W_0 @PBE bandgap, and E_o represents the position of the first prominent absorption peak obtained from the BSE/mBSE calculations [51, 52]. Table V indicates that the E_B values of these RP phases range from 0.17 to 0.33 eV, decreasing with increasing n . This trend aligns with the predictions of the Wannier-Mott model. Tables V and VI show that $E_B \gg \hbar\omega_{LO}$, indicating that the electronic contribution dominates over the ionic contribution in dielectric screening ($\varepsilon_{\text{eff}} \rightarrow \varepsilon_\infty$) for RP phases. The studies also reveal that the E_B values of these RP phases are generally smaller compared to their bulk counterparts ($n = \infty$), with the exception of Ba-based compounds [13]. In view of this, the considered RP phases are anticipated to be superior optoelectronic materials compared to their bulk counterparts.

Table V. Excitonic parameters for $A_{n+1}\text{Hf}_n\text{S}_{3n+1}$ ($A = \text{Ca}, \text{Sr}, \text{Ba}$ and $n = 1-3$) RP phases using BSE/mBSE approach.

Configurations	E_B (eV)	T_{exc} (K)	r_{exc} (nm)	$ \phi_l(0) ^2$ ($10^{27}m^{-3}$)	$\frac{1}{ \phi_l(0) ^2}$ ($10^{-27}m^3$)	
$\text{Ca}_{n+1}\text{Hf}_n\text{S}_{3n+1}$	$n = 1$	0.24	2783	1.20	0.18	5.48
	$n = 2$	0.21	2435	0.94	0.38	2.64
	$n = 3$	0.17	1971	0.32	9.93	0.10
$\text{Sr}_{n+1}\text{Hf}_n\text{S}_{3n+1}$	$n = 1$	0.27	3130	1.17	0.20	5.04
	$n = 2$	0.26	3014	0.90	0.44	2.28
	$n = 3$	0.23	2667	0.38	6.00	0.17
$\text{Ba}_{n+1}\text{Hf}_n\text{S}_{3n+1}$	$n = 1$	0.33	3826	0.89	0.45	2.22
	$n = 2$	0.29	3362	0.71	0.89	1.12
	$n = 3$	0.23	2667	0.35	7.63	0.13

Next, additional excitonic parameters, including the excitonic temperature (T_{exc}), radius (r_{exc}), and probability of wave function ($|\phi_l(0)|^2$) for $e-h$ pair at zero separation, have been calculated (for details, see the Supplemental Material). The computed values of these parameters are presented in Table V. It is well established that the inverse of $|\phi_l(0)|^2$ serves as a qualitative indicator of exciton lifetime (τ_{exc} ; for details, see the Supplemental Material). Table V suggests that the value of $|\phi_l(0)|^2$ increases with increasing n in these RP phases. Consequently, the exciton lifetime (τ_{exc}) is expected to decrease with higher values of n in these phases. A longer exciton lifetime corresponds to a reduced carrier recombination rate, thereby enhancing the quantum yield and improving the conversion efficiency.

E. Polaronic Properties:

It is well known that polar materials frequently undergo polaron formation, which significantly affects the mobility of charge carriers. The Fröhlich model provides a comprehensive description of the interaction between charge carriers and polar lattice vibrations [53]. Fröhlich proposed a dimensionless descriptor, α , to quantify the strength of this interaction, as follows [48]:

$$\alpha = \frac{1}{4\pi\varepsilon_0} \frac{1}{2} \left(\frac{1}{\varepsilon_\infty} - \frac{1}{\varepsilon_s} \right) \frac{e^2}{\hbar\omega_{LO}} \left(\frac{2m^*\omega_{LO}}{\hbar} \right)^{1/2} \quad (3)$$

where ε_0 is the permittivity of free space, m^* represents the effective mass of the carrier, and ω_{LO} is the characteristic phonon angular frequency. The thermal "B" approach, developed by Hellwarth et al. [38], is used to determine ω_{LO} by averaging the spectral contributions of multiple phonon branches (for details, see the Supplemental Material).

The computed carrier-phonon coupling constants (α) for both electrons and holes in these RP phases are listed in Table VI. It is observed that the considered RP phases exhibit intermediate to strong carrier-phonon coupling, which is significant and cannot be neglected for these materials [54]. The Fröhlich model also reveals that, for these compounds, the hole-phonon coupling is significantly stronger than the electron-phonon coupling. Additionally, the Debye temperature (θ_D) for these RP phases is calculated and found to be lower than room temperature (except Ca_2HfS_4), suggesting a strong interaction between carriers and phonons.

Polaron formation notably causes a reduction in the quasiparticle (QP) energies of both electrons and holes. This polaron energy (E_p) can also be determined using the parameter α , as follows [48]:

$$E_p = (-\alpha - 0.0123\alpha^2)\hbar\omega_{LO} \quad (4)$$

Table VI indicates that the energy of the charge-separated polaronic states in these RP phases is lower than that of their bound exciton states. This implies that the charge-separated polaronic states are less stable compared to the bound excitons.

Further, based on the extended form of Fröhlich's polaron theory, as developed by Feynman, the effective mass of the polaron (m_p) is expressed as (for a small α) [55]:

$$m_p = m^* \left(1 + \frac{\alpha}{6} + \frac{\alpha^2}{40} + \dots \right) \quad (5)$$

The effective masses of electrons and holes increase due to polaron formation, with the extent of this increase quantified to range between 27% and 644% in these materials (see Table VI). These results demonstrate that electron-phonon coupling leads to a significant increase in the polaron effective mass, suggesting intermediate to strong carrier-lattice interactions. In addition, the upper bound of the charge-carrier mobilities (μ_p) for these RP phases is estimated using Feynman's variational solution to Fröhlich's polaron Hamiltonian and by integrating the polaron response function [38, 54, 55] (for details, see the Supplemental Material). The polaron mobility, as described by the Hellwarth polaron model, is defined as follows [38]:

$$\mu_p = \frac{(3\sqrt{\pi}e)}{2\pi c\omega_{LO}m^*\alpha} \frac{\sinh(\beta/2)}{\beta^{5/2}} \frac{w^3}{v^3} \frac{1}{K(a,b)} \quad (6)$$

where e denotes the electronic charge, $\beta = \hbar c\omega_{LO}/k_B T$, w and v both are the temperature-dependent variational parameters, and $K(a,b)$ is a function of β , w , and v (for details, see the Supplemental Material). Our findings (see Table VI) reveal that as n increases in the considered RP phases, the polaron mobility of electrons decreases, becoming very small in their bulk counterparts ($n = \infty$) [13]. In contrast, the polaron mobility of holes displays an oscillating behavior. The polaron mobility values span from 26.32 to 121.32 $\text{cm}^2\text{V}^{-1}\text{s}^{-1}$ for electrons and from 0.04 to 17.14 $\text{cm}^2\text{V}^{-1}\text{s}^{-1}$ for holes. In view of this, the considered RP phases are expected to be superior optoelectronic materials compared to their bulk counterparts.

Table VI. Polaron parameters for electrons (e) and holes (h) of $\text{A}_{n+1}\text{Hf}_n\text{S}_{3n+1}$ ($\text{A} = \text{Ca}, \text{Sr}, \text{Ba}$ and $n = 1-3$) RP phases.

Configurations	ω_{LO} (THz)	θ_D (K)	α		E_p (meV)		m_p/m^*		μ_p ($\text{cm}^2\text{V}^{-1}\text{s}^{-1}$)		
			e	h	e	h	e	h	e	h	
$\text{Ca}_{n+1}\text{Hf}_n\text{S}_{3n+1}$	$n = 1$	6.51	312.57	1.35	2.41	37.00	66.90	1.27	1.55	121.32	17.14
	$n = 2$	3.63	174.29	2.69	8.17	41.78	135.16	1.63	4.03	58.81	0.65
	$n = 3$	3.58	171.89	3.52	5.89	54.45	93.65	1.90	2.85	37.21	4.97
$\text{Sr}_{n+1}\text{Hf}_n\text{S}_{3n+1}$	$n = 1$	4.72	226.63	1.80	3.65	35.96	74.55	1.38	1.94	93.25	7.86
	$n = 2$	4.14	198.78	2.68	9.76	47.46	187.42	1.63	5.01	56.18	0.21
	$n = 3$	1.53	73.46	5.50	9.83	37.21	69.81	2.67	5.05	33.52	3.19
$\text{Ba}_{n+1}\text{Hf}_n\text{S}_{3n+1}$	$n = 1$	4.47	214.62	2.06	4.45	39.10	86.88	1.45	2.24	76.15	4.69
	$n = 2$	3.91	187.74	2.84	13.06	47.59	245.44	1.67	7.44	51.91	0.04
	$n = 3$	3.59	172.37	4.30	7.61	67.31	123.73	2.18	3.72	26.32	2.29

IV. CONCLUSIONS:

In conclusion, we have reported the ground- and excited-state properties of the RP phases of $\text{A}_{n+1}\text{Hf}_n\text{S}_{3n+1}$ (where $\text{A} = \text{Ca}, \text{Sr}, \text{Ba}$ and $n = 1-3$) using a combination of density functional theory and many-body perturbation theory.

Our study demonstrates that these RP phases are mechanically stable and exhibit ductile behavior. The $G_0W_0@PBE$ bandgaps (1.43–2.14 eV) of these RP phases are smaller than those of their bulk counterparts, while the low effective masses of electrons suggest excellent charge carrier mobility, beneficial for energy-harvesting applications. BSE and mBSE calculations further reveal that these materials have an optical bandgap in the visible region, with exciton binding energies (0.17–0.33 eV) decreasing as the perovskite layer thickness increases. We also observe a dominant electronic contribution and a negligible ionic contribution to the effective dielectric screening in these RP phases. In addition, by calculating the electron-phonon coupling parameters, we find that these compounds exhibit significant carrier-lattice interactions, with charge-separated polaronic states being less stable than the bound excitons. The Hellwarth polaron model predicts that these RP phases exhibit higher polaronic mobility of electrons (26.32–121.32 $\text{cm}^2\text{V}^{-1}\text{s}^{-1}$) compared to their bulk counterparts. Overall, these results are anticipated to accelerate the research and adoption of RP phases in optoelectronic applications.

ACKNOWLEDGMENTS

S.A. would like to acknowledge the Council of Scientific and Industrial Research (CSIR), Government of India [Grant No. 09/1128(11453)/2021-EMR-I] for Senior Research Fellowship. The authors acknowledge the High Performance Computing Cluster (HPCC) ‘Magus’ at Shiv Nadar Institution of Eminence for providing computational resources that have contributed to the research results reported within this paper.

-
- [1] A. Kojima, K. Teshima, Y. Shirai, and T. Miyasaka, *J. Am. Chem. Soc.* **131**, 6050 (2009), <https://doi.org/10.1021/ja809598r>.
- [2] NREL, Photovoltaic Research (2024).
- [3] N.-G. Park, *J. Phys. Chem. Lett.* **4**, 2423 (2013), <https://doi.org/10.1021/jz400892a>.
- [4] J. Berry, T. Buonassisi, D. A. Egger, G. Hodes, L. Kronik, Y.-L. Loo, I. Lubomirsky, S. R. Marder, Y. Mastai, J. S. Miller, D. B. Mitzi, Y. Paz, A. M. Rappe, I. Riess, B. Rybtchinski, O. Stafsudd, V. Stevanovic, M. F. Toney, D. Zitoun, A. Kahn, D. Ginley, and D. Cahen, *Adv. Mater.* **27**, 5102 (2015), <https://onlinelibrary.wiley.com/doi/pdf/10.1002/adma.201502294>.
- [5] D. A. Egger, A. M. Rappe, and L. Kronik, *Acc. Chem. Res.* **49**, 573 (2016), <https://doi.org/10.1021/acs.accounts.5b00540>.
- [6] D. B. Straus, S. Guo, A. M. Abeykoon, and R. J. Cava, *Adv. Mater.* **32**, 2001069 (2020), <https://onlinelibrary.wiley.com/doi/pdf/10.1002/adma.202001069>.
- [7] A. Babayigit, A. Ethirajan, M. Muller, and B. Conings, *Nat. Mater.* **15**, 247 (2016).
- [8] D. Tiwari, O. S. Hutter, and G. Longo, *J. Phys. Energy* **3**, 034010 (2021).
- [9] S. Niu, H. Huyan, Y. Liu, M. Yeung, K. Ye, L. Blankemeier, T. Orvis, D. Sarkar, D. J. Singh, R. Kapadia, and J. Ravichandran, *Adv. Mater.* **29**, 1604733 (2017), <https://onlinelibrary.wiley.com/doi/pdf/10.1002/adma.201604733>.
- [10] X. Wu, W. Gao, J. Chai, C. Ming, M. Chen, H. Zeng, P. Zhang, S. Zhang, and Y.-Y. Sun, *Sci. China Mater.* **64**, 2976 (2021).
- [11] Y.-Y. Sun, M. L. Agiorgousis, P. Zhang, and S. Zhang, *Nano Lett.* **15**, 581 (2015), <https://doi.org/10.1021/nl504046x>.
- [12] M. Kumar, A. Singh, D. Gill, and S. Bhattacharya, *J. Phys. Chem. Lett.* **12**, 5301 (2021).
- [13] P. Basera and S. Bhattacharya, *J. Phys. Chem. Lett.* **13**, 6439 (2022), <https://doi.org/10.1021/acs.jpcclett.2c01337>.
- [14] R. Lelieveld and D. J. W. IJdo, *Acta Cryst. B* **36**, 2223 (1980).
- [15] S. Kong, H. Dong, Z. Yu, J. Guo, K. Cao, K. Chen, X. Ke, C. Zhou, J. Deng, S. Yang, and Y. Zhang, *Ceram. Int.* **50**, 10889 (2024).
- [16] R. Chami, A. Lekdadri, L. Omari, E. Hlil, and M. Chafi, *Mater. Today Energy* **20**, 100689 (2021).
- [17] D. Liu, H. Peng, J. He, and R. Sa, *Mater. Sci. Semicond. Process.* **169**, 107919 (2024).
- [18] D. L. Rode and P. A. Fedders, *J. Appl. Phys.* **54**, 6425 (1983).
- [19] S. B. Ogale and A. Madhukar, *J. Appl. Phys.* **56**, 368 (1984).
- [20] Q. Sun, H. Chen, and W.-J. Yin, *Chem. Mater.* **31**, 244 (2019), <https://doi.org/10.1021/acs.chemmater.8b04320>.
- [21] W. Li, S. Niu, B. Zhao, R. Haiges, Z. Zhang, J. Ravichandran, and A. Janotti, *Phys. Rev. Mater.* **3**, 101601 (2019).
- [22] Y. Zhang, M. P. K. Sahoo, Y. Liang, and G. Tang, *J. Phys. Chem. Lett.* **13**, 9632 (2022).
- [23] D. Gill, A. Singh, M. Jain, and S. Bhattacharya, *J. Phys. Chem. Lett.* **12**, 6698 (2021).
- [24] Y. Zhang, T. Shimada, T. Kitamura, and J. Wang, *J. Phys. Chem. Lett.* **8**, 5834 (2017), <https://doi.org/10.1021/acs.jpcclett.7b02591>.
- [25] C. C. Stoumpos, D. H. Cao, D. J. Clark, J. Young, J. M. Rondinelli, J. I. Jang, J. T. Hupp, and M. G. Kanatzidis, *Chem. Mater.* **28**, 2852 (2016).
- [26] P. Hohenberg and W. Kohn, *Phys. Rev.* **136**, B864 (1964).
- [27] W. Kohn and L. J. Sham, *Phys. Rev.* **140**, A1133 (1965).
- [28] H. Jiang, P. Rinke, and M. Scheffler, *Phys. Rev. B* **86**, 125115 (2012).
- [29] F. Fuchs, C. Rödl, A. Schleife, and F. Bechstedt, *Phys. Rev. B* **78**, 085103 (2008).

- [30] J. P. Perdew, K. Burke, and M. Ernzerhof, *Phys. Rev. Lett.* **77**, 3865 (1996).
- [31] J. Heyd, G. E. Scuseria, and M. Ernzerhof, *J. Chem. Phys.* **118**, 8207 (2003).
- [32] L. Hedin, *Phys. Rev.* **139**, A796 (1965).
- [33] M. S. Hybertsen and S. G. Louie, *Phys. Rev. Lett.* **55**, 1418 (1985).
- [34] S. Albrecht, L. Reining, R. Del Sole, and G. Onida, *Phys. Rev. Lett.* **80**, 4510 (1998).
- [35] M. Rohlfing and S. G. Louie, *Phys. Rev. Lett.* **81**, 2312 (1998).
- [36] M. Bokdam, T. Sander, A. Stroppa, S. Picozzi, D. D. Sarma, C. Franchini, and G. Kresse, *Sci. Rep.* **6**, 28618 (2016).
- [37] Y. Cho and T. C. Berkelbach, *J. Phys. Chem. Lett.* **10**, 6189 (2019).
- [38] R. W. Hellwarth and I. Biaggio, *Phys. Rev. B* **60**, 299 (1999).
- [39] P. E. Blöchl, *Phys. Rev. B* **50**, 17953 (1994).
- [40] G. Kresse and J. Furthmüller, *Phys. Rev. B* **54**, 11169 (1996).
- [41] G. Kresse and J. Furthmüller, *Comput. Mater. Sci.* **6**, 15 (1996).
- [42] K. Momma and F. Izumi, *J. Appl. Crystallogr.* **44**, 1272 (2011).
- [43] A. M. Ganose, A. J. Jackson, and D. O. Scanlon, *J. Open Source Softw.* **3**, 717 (2018).
- [44] M. Gajdoš, K. Hummer, G. Kresse, J. Furthmüller, and F. Bechstedt, *Phys. Rev. B* **73**, 045112 (2006).
- [45] S. Ruddlesden and P. Popper, *Acta Crystallogr.* **11**, 54 (1958).
- [46] F. Mouhat and F.-X. Coudert, *Phys. Rev. B* **90**, 224104 (2014).
- [47] S. Pugh, London, *Edinburgh Dublin Philos. Mag. J. Sci.* **45**, 823 (1954).
- [48] S. Adhikari and P. Johari, *Phys. Rev. B* **109**, 174114 (2024).
- [49] C. Freysoldt, B. Grabowski, T. Hickel, J. Neugebauer, G. Kresse, A. Janotti, and C. G. Van de Walle, *Rev. Mod. Phys.* **86**, 253 (2014).
- [50] C. D. Spataru and F. Leonard, *Chem. Phys.* **413**, 81 (2013).
- [51] X. Wang, W. Meng, and Y. Yan, *J. Appl. Phys.* **122**, 085104 (2017), <https://doi.org/10.1063/1.4991913>.
- [52] S. Adhikari and P. Johari, *Phys. Rev. B* **110**, 014101 (2024).
- [53] H. Fröhlich, *Adv. Phys.* **3**, 325 (1954), <https://doi.org/10.1080/00018735400101213>.
- [54] J. M. Frost, *Phys. Rev. B* **96**, 195202 (2017).
- [55] R. P. Feynman, *Phys. Rev.* **97**, 660 (1955).